

Finite Fault Analysis and Near Field Dynamic Strains and Rotations due to the 11/05/2011 (Mw5.2) Lorca Earthquake, South-Eastern Spain.

by Miguel A. Santoyo¹

¹. Departamento de Geofísica y Meteorología, Facultad de Ciencias Físicas, Universidad Complutense de Madrid. Plaza de Ciencias s/n, Ciudad Universitaria, 28040, Madrid, Spain. e-mail: masantoyo@pdi.ucm.es .

ABSTRACT

The 11/5/2011 Lorca, Spain earthquake (Mw=5.2) and its foreshock produced extensive damage to buildings and infrastructures within the town of Lorca and vicinity. During these earthquakes, evidence of rotational behaviour and permanent deformations in many structures were observed. The closest accelerometric station that recorded the ground motions was located about 6.0 km from the hypocentral zone. To analyze these aspects and study the source properties from the near-field, I obtained by an appropriate double time-integration procedure of accelerograms, the displacement time histories including the static component. Using these data I calculated the foreshock and the mainshock slip distributions by means of a complete waveform kinematic inversion. To study the dynamic deformations, the 3D tensor of displacement gradients at Lorca station was computed by a single station method. This was done assuming the incidence of body waves at the recording location. Using the finite fault inversion results and a first order finite difference approach, I calculated the 3D tensor of synthetic dynamic deformations at surface in the same site. Synthetic Green's functions were computed using the discrete wave-number method. After comparing the results from both methods, I extended the computation to the close neighboring area of the town, in order to infer the peak dynamic deformations distribution at surface. This was done calculating a surface array of synthetic dynamic strains and rotations in the close area of the recording place. The possible influence of the near-field deformations on the surface structures was finally analyzed.

Keywords: Lorca 2011 earthquake. Finite fault inversion. Slip Distribution. Dynamic strains and rotations.

INTRODUCTION

The 11/5/2011 Lorca, Spain earthquake (Mw=5.2) showed with severity the damaging potential of relatively small shallow earthquakes rupturing near populated areas. During this seismic series, 9 people died and about 300 people were injured. Extensive damages to historical and recently constructed buildings were produced within the urban area, including several partial and total collapses of buildings and churches (Feriche 2011; Giner-Robles 2011; IGN 2011). Among others, strong structural damages on buildings like large permanent deformations of ground floor storeys, shear failures on columns and cracks on bearing walls were extensively observed (e.g. Vidal et al. 2011; Murphy 2011). Possible geotechnical failures were also recognized (Vidal et al. 2011). Non-structural damages included the extensive falling of parapets and external masonry panels. A special attention was given to the observational evidence of possible rotational effects on structures. Examples of this were the permanent rotations observed after the earthquakes on some blocks of an obelisk, and the rotation of spires or pinnacles at the top of some church towers (Feriche 2011; Vidal et al. 2011). Giner-Robles et al. (2011) reported strong permanent deformations on historical structures including torsions on several church bell-towers.

Some damaging effects produced by earthquakes may be a direct result of high dynamic deformations (strains and rotations) rather than from peak accelerations or other displacement variations (e.g. Clough and Penzien 1993; Bodin et al. 1997; Stupatzzini et al. 2009). An example of this were the strong damages suffered by the Mexico City's water system following the September 19, 1985 Mexico earthquake Mw8.1 (Ayala and O'Rourke 1989). Surface

dynamic deformations induced by earthquakes have been studied in the past for different regions (e.g. Spudich et al. 1995; Bodin et al. 1997; Gomberg 1997; Spudich and Fletcher 2008). Pioneering works (e.g. Luco and Storipoulos 1980; Bouchon and Aki 1982; Lee and Trifunac 1985; Lee and Trifunac 1987) have showed that rotational ground motions can be important in the near-field. After them, the rotational effects induced by earthquakes have been gaining interest among the scientific community (e.g. Lee et al. 2009). As recent examples, Stupatzzini et al. (2009) studied the rotational ground motion effects in the near-field region for the Grenoble Valley and Cucci and Tertuliani (2011) studied the rotational effects due to the L'Aquila 2009 earthquake in Italy.

In this work, using the displacement time histories due to the 2011 Lorca Mw=5.2 mainshock and Mw=4.6 foreshock, I performed a linear kinematic inversion of complete waveforms for the finite rupture slip distribution on the fault plane. After this, I computed the 3D tensor of dynamic deformations from data, by the aid of a single station method assuming the incidence of body waves through the closest recording site. Using the obtained finite fault results and by means of a first order finite difference approach for the computation of the spatial derivatives of ground motion, I computed the 3D tensor of synthetic dynamic deformations at surface. After comparing the results from both methods, I extended the analysis to the neighboring area of the town, in order to estimate the peak dynamic deformation distribution at surface. The possible influence of these free-field deformations in the urban area was analyzed.

Tectonic setting and recent seismicity.

Seismicity in southern Spain is mainly governed by the convergence between the African plate and the Eurasian plate and characterized by low to moderate earthquake magnitudes. In the western Mediterranean, the relative velocity between the African plate with respect to the Eurasian plate varies between 4 mm-yr⁻¹ and 9 mm-yr⁻¹ (e.g. Nocquet and Calais 2003).

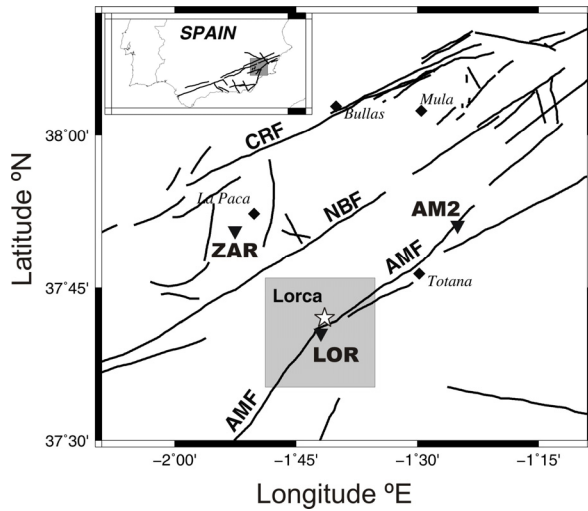


Figure 1. Location map and tectonic setting of the studied area. Solid lines indicate the trace of the main faults in the region. CRF =Crevillente fault; NBF =North-Betic fault; AMF=Alhama de Murcia fault. Solid triangles show the location of accelerometric stations: LOR=Lorca; ZAR= Zarcilla de Ramos; AM2= Alhama de Murcia. Solid diamonds indicate the location of near towns. White star show the location of the 11/5/2011 (Mw5.2) mainshock. Gray rectangle shows the area for computations of surface dynamic deformations. Inset: General location map of the study area in Spain.

The Murcia region is located in the eastern side of the Betics Cordillera in the western part of the European Alpine chain. The Betics are divided in the Internal and the External zones, whose contact is formed by a rather complicated tectonic setting composed by different fault systems. One of the main systems in this boundary strip is the Alhama de Murcia Fault (AMF; Figure 1) (e.g. Martinez-Díaz 2002). The principal directions of its surface expressions are oriented between the azimuths 40° and 80° (Martinez-Díaz 2002). Different fault systems including the AMF have been associated with the seismicity in this zone, characterized by focal mechanisms ranging from pure strike slip to steep thrusting at shallow depths (e.g. Buforn et al. 1995). Since the middle of the past century, several moderate earthquakes ($M > 5$) have occurred in this region. Between 1995 and 2010, four seismic series have taken place in this zone: the 1995 (Mw4.1) and 1999 (Mw4.9) Mula series, the 2002 (Mw5.0) Bullas series and the 2005 Bullas–La Paca (Mw4.7) series (e.g. Santoyo and Luzón 2008).

The 11/5/2011 (Mw5.2) Lorca earthquake series has been attributed to the AMF system activity (Martinez-Díaz 2011;

Vissers and Meijninger 2011). The foreshock and mainshock locations were preliminary estimated about 3.0–6.0 km E-NE the town of Lorca (IGN 2011). The foreshock, mainshock and major aftershock depths were preliminary set between 1.0km and 6.0km. At least, 47 regional broad-band and 13 accelerometric stations recorded the three main events of the series. From them, the closest recording site was the Lorca accelerographic station, located few kilometres from the epicenter. Due to its proximity to the ruptured fault, relatively high peak horizontal accelerations (0.367g) were observed during the mainshock. Lopez-Comino et al. (2012) relocated the series including the three major events, analyzed their focal mechanisms and obtained the rupture directivity of the mainshock. They obtained a mean apparent source time function duration of 1.0s with its rupture towards the SW.

Data and finite source analysis

Accelerations taken at close distances from the source give an invaluable opportunity to study the strong motion in a wide range of frequencies, including the static component of displacement. Here I analyzed the recordings due to the two largest events (foreshock and mainshock), obtained by the accelerometric stations located within 25.0 km from the epicentral area (LOR, ZAR and AM2; Figure 1). Acceleration time histories were integrated two times following the procedure proposed by Iwan et al. (1985) and Zhu (2003). Due to its proximity from the source and the signal-to-noise ratio of accelerograms, an additional 3-pole Butterworth low-pass filtering with $f_c=15.0$ Hz was applied to the data (Boore and Bommer 2005). This procedure allows obtaining among others, the static component (permanent displacement) of the ground shaking. After the analysis, the near-field information was feasible to be recovered only from the recordings at LOR. ZAR and AM2 stations presented strong path- and site-effects. Given this, and in order to keep these effects from being transferred by the inversion into the slip distribution, I performed the analysis for both earthquakes using the three components from LOR. The accelerometer of this station is oriented N30°W (Alcalde, personal communication 2012).

Table 1.
CRUSTAL VELOCITY STRUCTURE USED IN THIS STUDY.

#	h	v_p	v_s	ρ	Q_p	Q_s
1	2.0	4.50	2.60	2.10	400	200
2	3.0	5.20	3.10	2.40	400	200
3	5.0	5.40	3.20	2.40	400	200
4	15.0	6.12	3.60	2.80	800	400
5	10.0	6.57	3.80	2.80	800	400
6	∞	7.76	4.50	2.90	800	400

Notes: # = layer number; h = layer thickness (km); v_p = P wave velocity (km/s); v_s = S wave velocity (km/s); ρ = mass density (g/cm³); Q_p = Quality factor for P waves; Q_s = Quality factor for S waves. Layer 6 corresponds to the Halfspace.

Due to this, in order to obtain the NS and EW displacements, the horizontal components were clockwise rotated 30° before the inversion. The mainshock largest displacements (3.5cm) were found on the N-S component of this station, with a permanent displacement of 1.2cm in

the southern sense. A vertical permanent displacement of 0.8cm was found on the vertical component in upward sense. The EW permanent displacements obtained have amplitudes below the noise level.

To study the finite fault characteristics of the ruptures, I performed a finite fault linear kinematic inversion of the displacement waveforms to obtain the fault slip distribution. Due to the proximity of their hypocenters and the similarities among their acceleration waveforms, both analyzed events were assumed to occur over the same fault plane. For the inversion I set a rectangular fault of 4.0km x 4.0km in strike and dip directions respectively, fitting the rupture area of both events. The fault plane was discretized into 289 square subfaults of equal size (0.25km x 0.25km) embedded in a horizontally layered earth structure. Each subfault was modeled by a double couple point source. For each point source the synthetic Green's functions at the recording site were computed using the discrete wavenumber method described by Bouchon and Aki (1977) and Bouchon (1979). The crustal velocity structure in the vicinity of the source region was taken from Corchete and Chourak (2009) for the Murcia region (Table 1). From here, the observed data together with the synthetic seismograms form an over-determined linear system of the type $\mathbf{AX}\approx\mathbf{B}$. Matrix \mathbf{A} contains the synthetic seismograms with its respective time delay due to the rupture velocity, \mathbf{B} is a vector with the observed records and \mathbf{X} is the solution vector containing the dislocation weighting values for the slip of each subfault. A more detailed description of the inversion procedure can be found in Santoyo et al. (2005), which follows the methodology by Hartzell and Heaton (1983), and Mendoza and Hartzell (1989). For the inversion it was assumed a constant rupture velocity of 2.6 km/s, which is 0.85 times the S wave velocity at the depth of the fault plane. A constant velocity implies that the rupture propagates with circular fronts. The hypocenter was located at the centre of the fault plane, and was assumed as the initiation point for the rupture. The location and depth of the mainshock hypocenter (37.727°N , 1.686°W , $Z=4.5\text{km}$) and the focal mechanism (Strike= 240° , Dip= 55° , Rake= 45°) were obtained from Lopez-Comino et al. (2012). This mechanism was also used to define the spatial setting of the fault plane (Strike= 240° , Dip= 55°). Rise time at each subfault was set to 0.15s in order to maintain a smooth rupture over the entire fault. During the inversion, the focal mechanism was kept the same for all subfaults as also the value of the rise time.

The resulting slip distribution for the foreshock and the mainshock and the comparison between the synthetics and the observed displacements are shown in Figures 2 and 3 respectively. Figure 2a shows the comparison for the foreshock displacements and Figures 2b and 2c the resulting slip distributions. In a similar way Figure 3a shows the comparison between the mainshock observed displacements and synthetics, and Figures 3b and 3c the resulting slip distributions.

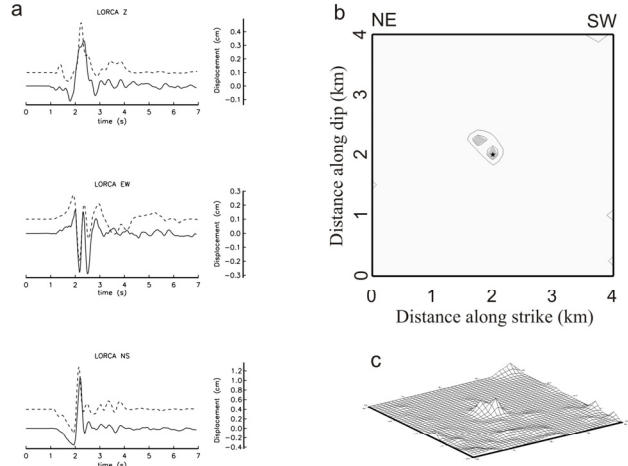


Figure 2

Figure 2. Results from the linear waveform inversion for the slip distribution due to the 11/5/2011 foreshock. **a.** Comparison between observed (solid) and synthetic (dashed) displacements at LOR in the NS (bottom), EW (middle) and vertical (top) directions. Displacement amplitudes are in cm. **b.** Slip distribution over the fault plane obtained from the linear kinematic inversion. Slips contours are shown every 20.0 cm, with a maximum slip of 45.0 cm. Fault plane is viewed from the NW. Black star shows the location of the epicentre and the initiation point for the rupture. Epicentre is at 4.5 km depth. **c.** Perspective view of the rupture amplitudes.

Here, a simple patch was obtained for the foreshock with a maximum slip of 45.0 cm and a static stress drop $\Delta\sigma\approx 450$ bar, assuming a circular fault. For the mainshock, two main patches were obtained. The maximum slip was on the north-eastern patch with a maximum of 135.0 cm. In this case, $\Delta\sigma\approx 280$ bar. Comparing the two obtained distributions, it appears that both events are complementary in their rupture areas, as it seems that no-overlapping exists between them. After inversion, the sense and amplitude of the static displacement agrees with the observed data, even in the case where the static displacements are relatively small. The rupture distribution in the mainshock partially agrees with the directivity obtained by Lopez-Comino et al. (2012), however in this case, rupture direction have a downdip propagation.

Methods for dynamic deformations.

Dynamic deformations using the Single Station method

The 3D tensor components of the dynamic deformations at surface were obtained from data by means of the single station method described in Gombert (1997) and Singh et al. (1997). In this method, the displacement gradients used to calculate the dynamic deformations are obtained assuming the incidence of body waves through the recording site. In this way assuming S waves incidence, the horizontal particle motion can be written as

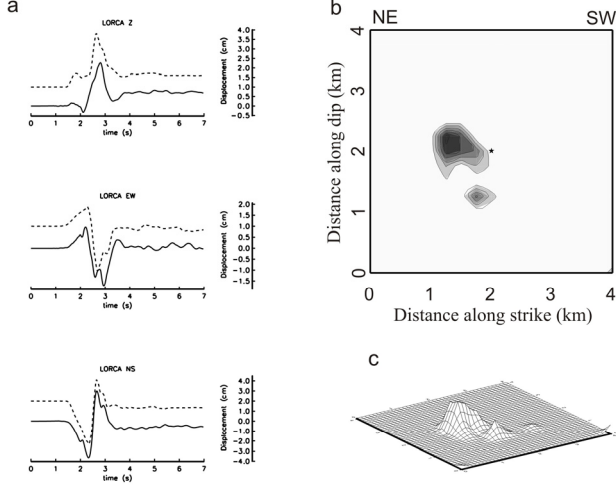


Figure 3

Figure 3. Results from the linear waveform inversion for the slip distribution due to the 11/5/2011 mainshock. **a.** Comparison between observed (solid) and synthetic (dashed) displacements at LOR in the NS (bottom), EW (middle) and vertical (top) directions. Displacement amplitudes are in cm. **b.** Slip distribution over the fault plane obtained from kinematic inversion. Slips are shown every 20 cm, with a maximum slip of 135.0 cm. Fault plane is viewed from the NW. Black star shows the location of the epicentre and the initiation point for the rupture. Epicentre is at 4.5 km depth. **c.** Perspective view of the rupture amplitudes.

$$u_{SH} = A_{SH} e^{i(\omega t - k_h \cdot r + \theta_{SH})} ; u_{SVh} = A_{SVh} e^{i(\omega t - k_h \cdot r + \theta_{SVh})}$$

$$\text{and } u_{SVv} = A_{SVv} e^{i(\omega t - k_h \cdot r + \theta_{SVv})} \quad (1)$$

where u_{SH} is the SH motion in the transverse direction, u_{SVb} and u_{SVv} are the SV motions in the radial and vertical direction respectively; A_{SH} , A_{SVb} and A_{SVv} are the amplitudes in the transverse, radial and vertical directions and θ_{SH} , θ_{SVb} , θ_{SVv} are the phases of the incident wavefield at the surface in the measurement point. $\omega = 2\pi f$ is the angular frequency and t = time. Here $\mathbf{k}_h \cdot \mathbf{r} = k_x x + k_y y$, where the magnitude of the horizontal wavenumber is $k_h = 2\pi/\lambda_b$ and λ_b is the horizontal wavelength. This one can be expressed as $\lambda_b = TV_s / \sin(\psi) = TV_b$, where T = period, V_s is the S wave velocity, V_b is the horizontal apparent velocity and ψ is the angle of wave incidence with respect to the vertical.

The horizontal surface motion can be resolved in the three Cartesian directions as (e.g. Gombert 1997)

$$u_j^x = A_j^x e^{i\theta_x} e^{i(\omega t - k_x x)} \quad \text{and} \quad u_j^y = A_j^y e^{i\theta_y} e^{i(\omega t - k_y y)} ;$$

$$j = x, y, z \quad (2)$$

The spatial derivatives of equations 2 are then taken in order to obtain the displacement gradients. The differentiation of the term $e^{-ik_x x}$ is equivalent to multiply by $-ik_x = -i2\pi/\lambda_x = -i(2\pi/\lambda_b) \sin(\phi)$ and the term $e^{-ik_y y}$ equivalent to multiply by $-ik_y = -i2\pi/\lambda_y =$

$-i(2\pi/\lambda_b) \cos(\phi)$, where ϕ is the angle of azimuth of the incidence wavefield. The derivative with respect to time is equivalent to multiplication in the frequency domain by $i2\pi/T$. From this, the spatial gradients G_{ij}^s (s for single station) of equations 2, at the measuring site can be written as:

$$U_x = \frac{\partial u_1}{\partial x_1} = -\frac{\partial u_1}{\partial t} \frac{\sin \phi}{V_h} = -\frac{\partial u_1}{\partial t} \frac{\sin \phi \sin \psi}{V_s} \quad (3)$$

$$V_x = \frac{\partial u_2}{\partial x_1} = -\frac{\partial u_2}{\partial t} \frac{\sin \phi}{V_h} = -\frac{\partial u_2}{\partial t} \frac{\sin \phi \sin \psi}{V_s}$$

$$W_x = \frac{\partial u_3}{\partial x_1} = -\frac{\partial u_3}{\partial t} \frac{\sin \phi}{V_h} = -\frac{\partial u_3}{\partial t} \frac{\sin \phi \sin \psi}{V_s}$$

$$U_y = \frac{\partial u_1}{\partial x_2} = -\frac{\partial u_1}{\partial t} \frac{\cos \phi}{V_h} = -\frac{\partial u_1}{\partial t} \frac{\cos \phi \sin \psi}{V_s}$$

$$V_y = \frac{\partial u_2}{\partial x_2} = -\frac{\partial u_2}{\partial t} \frac{\cos \phi}{V_h} = -\frac{\partial u_2}{\partial t} \frac{\cos \phi \sin \psi}{V_s}$$

$$W_y = \frac{\partial u_3}{\partial x_2} = -\frac{\partial u_3}{\partial t} \frac{\cos \phi}{V_h} = -\frac{\partial u_3}{\partial t} \frac{\cos \phi \sin \psi}{V_s}$$

Once obtained the components of G_{ij}^s , these were used to derive the uniform strains by means of

$$\varepsilon_{i,j} = \frac{1}{2} \left(\frac{\partial u_i}{\partial x_j} + \frac{\partial u_j}{\partial x_i} \right) \quad (4)$$

and the rigid body rotations by

$$\omega_{i,j} = \frac{1}{2} \left(\frac{\partial u_i}{\partial x_j} - \frac{\partial u_j}{\partial x_i} \right) \quad (5)$$

where $i=1,2,3$; $j=1,2,3$; $u_1=u$, $u_2=v$, $u_3=w$; u , v and w are the displacements in the \mathbf{x} , \mathbf{y} and \mathbf{z} directions at a given time. At the surface, due to the stress free boundary conditions, three components of G_{ij}^s are not independent: $\partial u_1 / \partial x_3 = -\partial u_3 / \partial x_1$, $\partial u_2 / \partial x_3 = -\partial u_3 / \partial x_2$ and $\partial u_3 / \partial x_3 = \eta (\partial u_2 / \partial x_2 + \partial u_1 / \partial x_1)$ and $\eta = \lambda / (\lambda + 2\mu)$; λ and μ are the Lamé parameters. From here, $\varepsilon_{1,3} = \varepsilon_{3,1} = \varepsilon_{2,3} = \varepsilon_{3,2} = 0$.

Dynamic deformations using a finite difference approach.

In order to infer the peak dynamic deformations in the Lorca urban area, I computed the 3D synthetic displacement gradients tensor terms at surface, first in the same recording site. This modeling was based on the slip distributions obtained above, and using a first-order finite difference scheme for the computation of the spatial derivatives of the ground motion.

In this way, the complete 3D tensor of synthetic displacement gradients $G_{ij}^s = \Delta u_i / \Delta x_j$, where Δu_i , $i=x,y,z$, (f for finite difference) are the differences in the synthetic displacements in the three spatial directions, and Δx_j , $j=1,2,3$ are the space increment in x , y and z directions respectively. The synthetic displacement time histories were computed by the discrete wave-number method (Bouchon 1979) within an area of 20 km x 20 km, and centered on the recording site. The spacing among computing points in

this case was taken as $\Delta x_j = \lambda_{\min}/100 = V_s/100f_N$, where $\Delta x_j = \Delta x_1 = \Delta x_2 = \Delta x_3$, V_s = minimum S wave velocity of the considered velocity structure, and f_N = maximum analyzed frequency. The time increment for this analysis $\Delta t = 1/f_s = 1/2f_N$, where $f_s = 40.0$ Hz is the sampling frequency of the observed seismograms. Once obtained all the terms of $G_{i,j}^f$, the components of the 3D synthetic strain tensor were obtained applying equations 4 and 5. Cotton and Coutant (1997) tested this methodology with respect to the solution using analytic spatial derivatives, obtaining undistinguishable results between both techniques.

To check that the waveforms resulting from both methods used here agrees in shape and amplitude, a quantitative comparison of the time histories was performed based on the misfit criterion:

$$m = 100 \frac{\sum_{k=1}^N \sqrt{[G_{i,j}^s(k\Delta t) - G_{i,j}^f(k\Delta t)]^2}}{A_{\max} \sqrt{N}}$$

where A_{\max} is the maximum absolute amplitude of the time histories from the single station method, Δt is the time increment and N is the total number of time samples (e.g. Martinez-Garz3n 2011). The computation of misfit was applied for a time window of 6.0 seconds after the first wave arrival.

Results and discussion

The wave incident angles ϕ and ψ at surface used for the single station method, were obtained taking into account the subsoil velocity structure and the relative location of the hypocenter with respect to the recording site. For each time, all the terms of the displacement gradient tensor were computed using equations 3. The four non-vanishing terms of the strain tensor and the three rotational components at surface were obtained using equations 4 and 5. The results of applying this method to the velocity data at LOR are shown in Figures 4 and 5 with solid lines. Figure 4 shows the four tensor terms of the uniform strains and the three tensor terms of rotations obtained from the foreshock recordings. Figure 5 shows in a similar way, the non-vanishing terms due to the mainshock event. Here the maximum amplitudes on the displacement gradients are mostly obtained on the horizontal components. The ϵ_{yy} term of uniform strains, systematically present the largest amplitudes. In the same way, rotation terms around the vertical axis are also larger than the ones around the horizontal axes. These results make sense due to the angle of incidence of the wave field, which in this case is highly vertical.

Figures 4 and 5 shows with dashed lines, the synthetic deformations obtained from applying the finite difference method to the foreshock and the mainshock slip distributions. After the misfit analyses, the differences from both methods gave relatively low values ($m < 5\%$) except in the tilt terms (rotations with respect to the horizontal axes) where differences were higher ($m < 25\%$). Given this, dynamic deformations in the vicinity of the recording station were analyzed taking into account these differences.

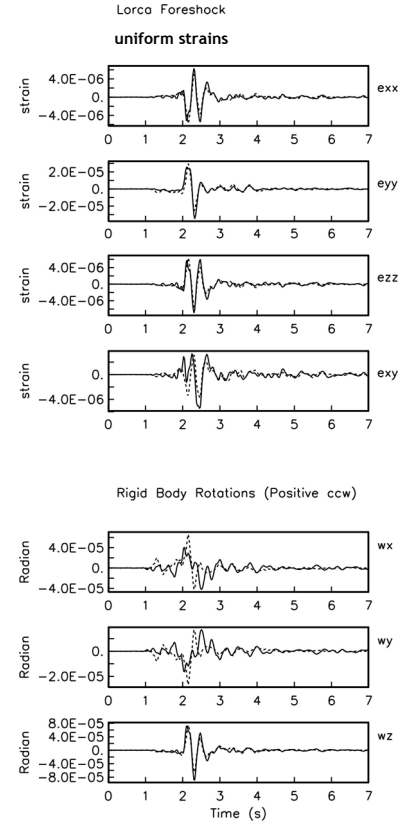


Figure 4

Figure 4. Foreshock dynamic strains and rotations at LOR station. Terms for the uniform strains ϵ_{11} , ϵ_{22} , ϵ_{33} and ϵ_{12} at the top of figure and ω_1 , ω_2 and ω_3 , at the bottom. Solid lines show the time histories from the single station method and dashed lines show histories from the finite difference modeling. Units for uniform strains are in strain, and radians for rigid body rotations.

Figures 6 and 7, shows the resulting distribution of surface peak-dynamic strains and rotations due to the mainshock. In these figures Lorca town contour is shown in solid brown. The aftershock locations relocated by Lopez-Comino et al. (2012) are shown with open dots. The surface projection of the fault plane with respect to the urban area is shown with a black rectangle. Figures 6a to 6f shows the negative and positive peak dynamic values of the strain tensor terms $\epsilon_{1,1}$, $\epsilon_{2,2}$ respectively.

Figures 6g and 6h shows the negative and positive values of $\epsilon_{3,3}$, $\epsilon_{1,2}$ respectively. In these figures, units are in strain. Colour scale is shown at the right hand side for each figure, where cold colours show the negative values and the warm colours the positive range. Figures 7a to 7d show the clockwise and counter-clockwise peak dynamic tilts in the x and y directions respectively. Figures 7e and 7f show the clockwise and counter-clockwise peak dynamic torsions (rotations along the vertical axis z). Here, units are in radians and the colour scale is shown at the right hand side of each map. Cold colours show the clockwise values and warm colours the counter-clockwise range.

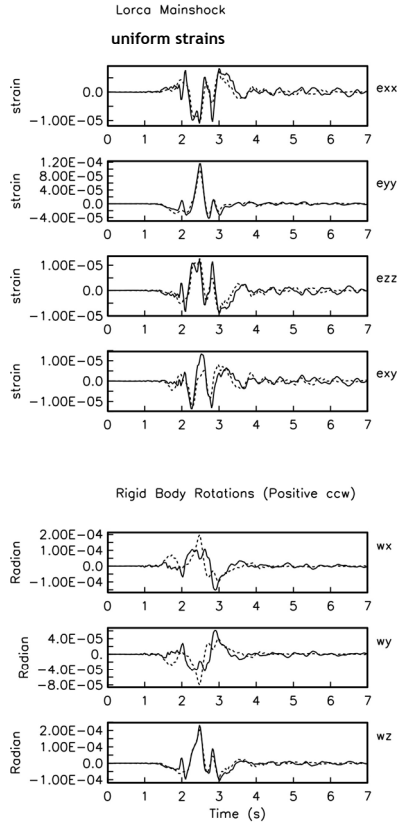


Figure 5

Figure 5. Mainshock dynamic strains and rotations at LOR station. Terms for the uniform strains ϵ_{11} , ϵ_{22} , ϵ_{33} and ϵ_{12} at the top of figure and ω_1 , ω_2 and ω_3 , at the bottom. Solid lines show the time histories from the single station method and dashed lines show histories from the finite difference modeling. Units for uniform strains are in strain, and radians for rigid body rotations.

From the maps showing the distribution of strain terms $\epsilon_{2,2}$, $\epsilon_{3,3}$ and $\epsilon_{1,2}$, it can be observed that the zones of maximum peak dynamic strains fall on the northern and southern sides from the ruptured fault. The southern zone appears to be coincident with the location of the urban area. Absolute values in these cases range in the urban area between 3.5×10^{-5} and 1.0×10^{-4} strain. The maximum peak dynamic strains corresponding to the term $\epsilon_{1,1}$ seems to occur on the south-western and north-eastern sides of the town. The order of magnitude of these strains, suggests that surface deformations may contribute to produce damages to shallow buried lifelines (e.g. Singh et al. 1997; Trifunac et al. 1996; Pineda-Porras and Najafi 2010).

On the other hand, distribution of tilts around the y axis seems to occur mainly in the eastern and western sides of the rupture; here the urban area appears to be in a low value zone. On the contrary, peak dynamic tilts around x axis and peak dynamic torsions could have their maximums near the town zone. Absolute values on tilts for this case are not reliable. Maximum peak torsions in some parts of the urban area could reach values of 3.0×10^{-4} radians. In the same sense, the counter-clockwise and clockwise rotations are in the urban area of the same order of magnitude. Due to this, a direct relation between these results and the observed rotations would be difficult to achieve. This task

could have additional difficulties because translational motions can produce some amount of the observed permanent rotations (e.g. Hinzen 2012).

Relative amplitudes of deformations however, can give some clues about the possible distribution of them in the near region from the fault at surface. The disagreement found on tilts could be possibly attributed to 2D or 3D propagation effects. E.g. Sanchez-Sesma and Campillo (1991) show that effects of topography on local wave amplification could be, under some circumstances, much larger on the horizontal directions. On the other hand, possible better adjustments on these terms could be reached performing a non-linear kinematic inversion, or by obtaining a more detailed relocation of the fault plane. Given the size of the studied earthquakes, a non-linear analysis was not the first-election inversion procedure, because this could introduce additional complexities on slips that may not be real.

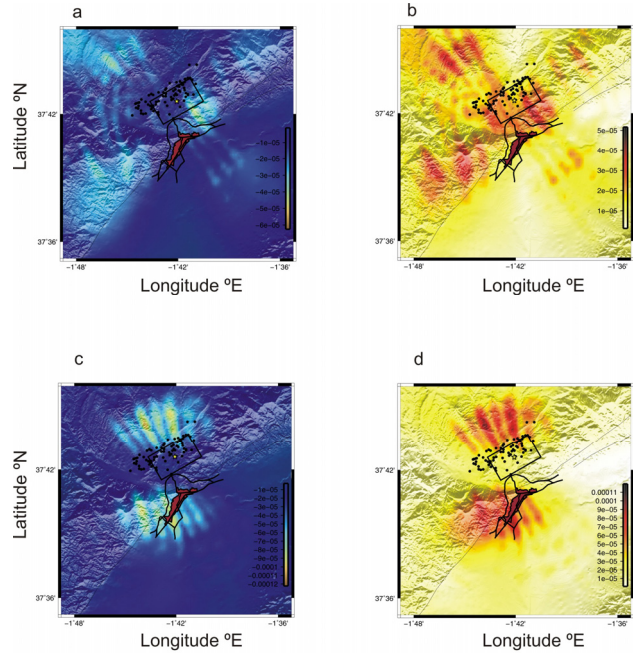


Figure 6

Figure 6. Mainshock peak dynamic strain maps at the surface. Lorca urban area contour is shown in solid brown. Relocated aftershock locations are shown with open dots. The surface projection of the fault plane with respect to the urban area is shown with a black rectangle. **a** and **b.** Negative and positive peak dynamic values of the strain tensor term $\epsilon_{1,1}$ respectively. **c** and **d.** Negative and positive peak dynamic values of $\epsilon_{2,2}$ **e** and **f.** Negative and positive values of $\epsilon_{3,3}$. **g** and **h.** Negative and positive peak dynamic values of $\epsilon_{1,2}$ respectively. In all cases units are in strain. Colour scale is shown at the right hand side of each map, where cold colours show the negative values and the warm colours the positive range.

CONCLUSIONS

Slip distributions obtained from kinematic inversion suggest that the two analyzed events, i.e. the M4.6 foreshock and the M5.2 mainshock, may have complementary ruptures as they are not overlapped. A

more detailed analysis by stress transfer computations over the fault plane could be realized in order to study the possible stress triggering of the mainshock due to the previous event. In any case, this kind of analysis was outside the scope of this work. Slip distributions show for the first event, a single ruptured patch with a maximum slip of 45.0 cm. For the second event two main patches were obtained with a maximum slip of 135.0 cm.

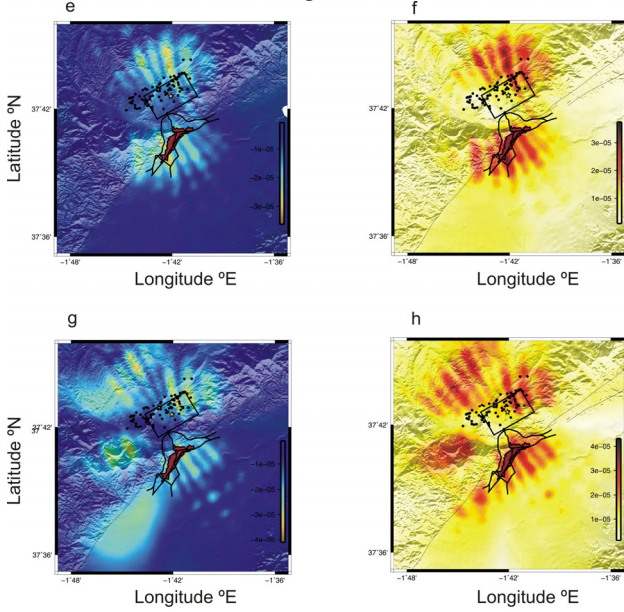


Figure 6 (cont)

Peak dynamic strains at the Lorca accelerometric station could reach values of the order of 1.2×10^{-4} strain, especially on the $\epsilon_{2,2}$ term of the dynamic tensor, and values of 2.0×10^{-4} radians in the ω_3 term. The order of magnitude of these values suggests that surface strains could contribute to produce damage to some shallow buried lifelines. On the other hand, the obtained absolute values on torsions could contribute to increase the rotational effects on structures.

Maximum peak dynamic strain terms $\epsilon_{2,2}$, $\epsilon_{3,3}$ and $\epsilon_{1,2}$, seems that occurred in the same zone of the urban area of Lorca. The same situation occurs with the rotational terms ω_1 , ω_3 where maximum peak dynamic rotations appear to occur also near the urban area.

Relative values of strains and rotations can give clues about the behaviour of dynamic strains and rotations experimented in the vicinity of the Lorca town during the Mw5.2 mainshock and the Mw4.6 foreshock. However its effects on the observed structural damages should be more investigated.

Acknowledgments

Accelerometric data were supplied by the Instituto Geográfico Nacional de España (IGN). I wish to thank Resurrección Antón and Juan Manuel Alcalde from IGN for their kind assistance in downloading the seismic data. Thanks to José Morales from Instituto Andaluz de Geofísica for providing the relocated seismicity. Fruitful discussions with Jorge M. Gaspar-Escribano and Miguel

Herraz helped to improve this work. Ligia E. Quiroz and Patricia Martínez-Garzón helped in part of the analysis of the theoretical deformations. DEGTRA-A4 program was used to process the accelerometric data. Axitra program by O. Coutant was used for the computation of Green's Functions. This work was done while the author M.A.S. was under the Subprogram Ramón y Cajal contract, of the Ministerio de Economía y Competitividad, Spain, supported by the European Social Fund.

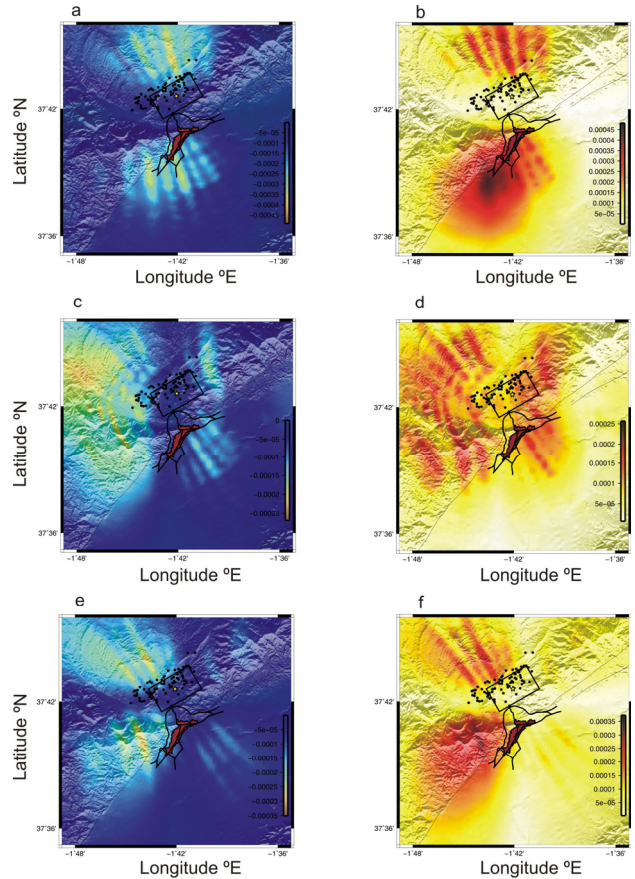


Figure 7

Figure 7. Mainshock peak dynamic rotation maps at surface. Lorca urban area contour is shown in solid brown. Relocated aftershock locations are shown with open dots. The surface projection of the fault plane with respect to the urban area is shown with a black rectangle. **a** and **b.** Clockwise and counter-clockwise peak dynamic tilts (rotations with respect to the horizontal axis) in x direction. **c** and **d.** Clockwise and counter-clockwise peak dynamic tilts in y direction. **e** and **f.** Clockwise and counter-clockwise peak dynamic torsions (rotations along the vertical axis z). Units in all cases are in radian. Colour scale is shown at the right hand side of each map. Cold colours show the clockwise values and warm colours the counter-clockwise range.

REFERENCES

- Alcalde J.M. (2012) Personal communication. Head of the Accelerographic Network, IGN, Spain.
- Ayala A. G., O'Rourke M. J. (1989) Effects of the 1985 Michoacan Earthquake on water systems and other buried lifelines in Mexico. National Center for Earthquake Engineering Research, State University of New York at Buffalo. Technical Report NCEER-89-0009, 120 pp.

- Bodin P., Gomberg J., Singh S. K., Santoyo M. (1997) Dynamic deformations of shallow sediments in the Valley of Mexico, Part I: Three-dimensional strains and rotations recorded on a seismic array. *Bull. Seism. Soc. Am.*, 87, 528-539.
- Boore D. M., Bommer J. J. (2005) Processing of strong-motion accelerograms: needs, options and consequences. *Soil Dyn. Earthq. Eng.*, 25, 93-115.
- Bouchon M. (1979) Discrete wave number representation of elastic wave field in three space dimensions. *J. Geophys. Res.*, 84, 3609-3614.
- Bouchon M., Aki K. (1977) Discrete wave number representation of seismic source wave fields. *Bull. Seism. Soc. Am.*, 67, 259-277.
- Bouchon M., Aki K. (1982) Strain, tilt, and rotation associated with strong ground motion in the vicinity of earthquake faults. *Bull. Seism. Soc. Am.*, 72, 1717-1738.
- Bufo E., Sanz de Galdeano C., Udias A. (1995) Seismotectonics of the Ibero-Maghrebian region. *Tectonophysics*, 248, 247-261.
- Clough R. W., Penzien J. (1993) *Dynamics of Structures*. B. J. Clark (Ed), Chap. 27, McGraw-Hill, New York, 704-710.
- Corchete V., Chourak M. (2009) Shear-wave velocity structure of the south-eastern part of the Iberian Peninsula from Rayleigh wave analysis. *Intern. J. Earth Sci.*, 100, 1733-1747.
- Cotton F., Coutant O. (1997) Dynamic stress variations due to shear faults in a plane-layered medium. *Geophys. J. Int.*, 128, 676-688.
- Cucci L., Tertulliani A. (2011) Clues for a relation between rotational effects induced by the Mw6.3 2009 L'Aquila (Central Italy) earthquake and site and source effects. *Bull. Seism. Soc. Am.*, 101-3, 1109-1120, doi: 10.1785/0120100264.
- Giner Robles J. L., Rodríguez Pascua M. A., Pérez López R., Martín-González F. (2011) Study of the historical building damage within the village using structural geology techniques. Testing the Archaeoseismology methods. In *Geological preliminary field report of the Lorca earthquake (5.1 Mw, 11th may 2011)*, Instituto Geológico y Minero de España. Internal Report. <http://www.igme.es>. Accessed 14 february 2012.
- Gomberg J. (1997) Dynamic deformations and the M6.7, Northridge, California earthquake. *Soil Dynam. Earthq. Eng.*, 16, 471-494. doi: 10.1016/S0267-7261(97)00011-0
- Hartzell S. H., Heaton T. H. (1983) Inversion of strong ground motion and teleseismic waveform data, for the fault rupture history of the 1979 Imperial Valley, California, earthquake. *Bull. Seism. Soc. Am.*, 76, 1553-1583.
- Hinzen K. G. (2012) Rotation of vertically oriented objects during earthquakes. *J. Seismol.* First online. DOI: 10.1007/s10950-011-9255-6
- Ferliche M. (2011) Efectos del terremoto de Lorca en las Edificaciones. Instituto Andaluz de Geofísica. <http://www.ugr.es/~iag>. Accessed 20 ocober 2011.
- IGN (2011) Serie terremoto NE Lorca (Murcia). Instituto Geográfico Nacional, <http://www.ign.es>. Accessed 14 february, 2012.
- Iwan W. D., Moser M. A., Peng C.Y. (1985) Some observations on strong-motion earthquake measurement using a digital accelerometer. *Bull. Seism. Soc. Am.*, 75, 1225-1246.
- Lee V. W., Trifunac M. D. (1985) Torsional accelerograms. *Soil Dyn. Earthq. Eng.*, 4, 3, 132-142.
- Lee, V. W., Trifunac M. D. (1987) Rocking strong earthquake accelerations. *Soil Dyn. Earthq. Eng.*, 6, 75-89.
- Lee, W. H. K., Çelebi M., Todorovska M. I., H. Igel (2009) Introduction to the Special Issue on Rotational Seismology and Engineering Applications. *Bull. Seism. Soc. Am.* 99, 2B, 945-957, doi: 10.1785/0120080344
- López-Comino J.A., Mancilla F.L., Morales J., Stich D. (2012) Rupture directivity of the 2011, Mw 5.2 Lorca earthquake (Spain). *Geoph. Res. Lett.*, 39, L03301, 5 PP. doi:10.1029/2011GL050498 .
- Luco, J. E., Sotiropoulos D. A. (1980) Local characterization of free-field ground motion and effects of wave passage. *Bull. Seism. Soc. Am.*, 70, 2229-2244.
- Martínez-Díaz J.J. (2002) Stress field variation related to fault interaction in a reverse oblique-slip fault: the Alhama de Murcia fault, Betic Cordillera, Spain. *Tectonophysics* 356, 291-305.
- Martínez-Díaz J. J., Álvarez-Gómez J. A. (2011) Seismotectonic characterization of the seismic series of Lorca and geological analysis of the earthquake source. In *Geological preliminary field report of the Lorca earthquake (5.1 Mw, 11th may 2011)*, Instituto Geológico y Minero de España. Internal Report. <http://www.igme.es>. Accessed 14 february 2012.
- Martínez-Garzón P. (2011) Deformaciones dinámicas originadas por sismos en presas: Caso de la presa de Itoiz (Navarra). Master's Dissertation. Universidad Complutense de Madrid. Spain.
- Mendoza C., Hartzell S. (1989) Slip distribution of the 19 September 1985 Michoacan. Mexico, earthquake: Near-source and teleseismic constraints. *Bull. Seism. Soc. Am.*, 79, 655-669.

- Murphy P. (2011) Quick field report. Lorca earthquake 11th May 2011. Internal Report. Broadway Maylan. Madrid.
- Nocquet J.M., Calais E. (2003) Crustal velocity field of Western Europe from permanent GPS array solutions, 1996–2001. *Geophys. J. Int.*, 154, 72–88.
- Pineda-Porras O., Najafi M. (2010) Seismic Damage Estimation for Buried pipelines: challenges after three decades of progress. *J. Pipeline Sys. Eng. Pract.*, 1, 1, doi: 10.1061/(ASCE)PS.1949-1204.0000042.
- Sanchez-Sesma F. J., Campillo M. (1991) Diffraction of P, SV and Rayleigh waves by topographic features: a boundary integral formulation. *Bull. Seism. Soc. Am.*, 81, 2234-2253,
- Santoyo M.A., Luzón F. (2008) Stress relations in three recent seismic series in the Murcia region, southeastern Spain. *Tectonophysics*, 457, 86–95. doi: 10.1016/j.tecto.2008.05.019
- Santoyo M. A, Singh S. K., Mikumo T. (2005) Source process and stress change associated with the 11 January, 1997 (Mw=7.1) Michoacán, Mexico, inslab earthquake. *Geofís. Int.*, 44, 4, 317-330.
- Singh S. K., Santoyo M., Bodin P., Gomberg J. (1997) Dynamic deformations of shallow sediments in the valley of Mexico, Part II: single station estimates. *Bull. Seism. Soc. Am.*, 87, 540-550.
- Spudich P., Steck L. K., Hellweg M., Fletcher J. B., Baker L. (1995) Transient stresses at Parkfield, California, produced by the M 7.4 Landers earthquake of June 28, 1992: observations from the UPSAR dense seismograph array. *J. Geophys. Res.*, 100, 675-690.
- Spudich P., Fletcher J. B. (2008) Observation and prediction of dynamic ground strains, tilts and torsions caused by the M6.0, 2004 Parkfield, California, earthquake and aftershocks derived from UPSAR array observations. *Bull. Seism. Soc. Am.*, 98, 1898-1914
- Stupazzini M., De la Puente J., Smerzini C., Käser M., Igel H., Castellani A. (2009) Study of Rotational Ground Motion in the Near-Field Region. *Bull. Seism. Soc. Am.*, 99, 2B, 1271-1286, doi:10.1785/0120080153
- Trifunac M. D., Todorovska M. I., Ivanovic S. S. (1996) Peak velocities, and peak surface strains during Northridge, California earthquake of 17 January 1994. *Soil Dyn. Earthq. Eng.*, 15, 5, 301–310.
- Vissers R.L.M., Meijninger B.M.L. (2011) The 11 May 2011 earthquake at Lorca (SE Spain) viewed in a structural-tectonic context. *Solid Earth*, 2, 199-204.
- Vidal F., Alguacil G., Feriche M., Aranda C., Morales J., Stich D., Pérez-Muelas J., Benito J., López J.M. (2011) El terremoto de Lorca. Mayo 2011. Causas del Impacto y Primeras Medidas. Análisis Preliminar. Instituto Andaluz de Geofísica. www.ugr.es/~iag. Accessed 17 september 2011.
- Zhu L. (2003) Recovering permanent displacements from seismic records of the June 9, 1994 Bolivia deep earthquake. *Geophys. Res. Lett.*, 30, 14, 1740, doi:10.1029/2003GL017302,